

Phase Dependent Spectral Variability in 4U1907+09

Mallory S.E. Roberts¹, Peter F. Michelson

mallory@astro.stanford.edu, peterm@leland.stanford.edu

Department of Physics, Stanford University, Stanford, CA 94305

Denis A. Leahy

leahy@iras.ucalgary.ca

Dept. of Physics, University of Calgary, Calgary, Alberta, Canada T2N 1N4

Tony A. Hall², John P. Finley

hall@egret.sao.arizona.edu, finley@physics.purdue.edu

Department of Physics, Purdue University, West Lafayette, IN 47907

Lynn R. Cominsky

lynnr@charmian.sonoma.edu

Department of Physics and Astronomy, Sonoma State University, 1801 E. Cotati Ave, Rohnert Park, CA 94928

and

Radhika Srinivasan

rsriniva@mrsc.ucsf.edu

Department of Radiology/MRSC, UCSF, San Francisco, Ca.

ABSTRACT

We report on ASCA, RXTE, and archival observations of the high mass X-ray binary pulsar 4U1907+09. Spectral measurements of the absorption and flux were made at all phases of the X-ray pulsar orbit, including the first spectral measurements of an extended period of low flux during two of the ASCA observations. We find that a simple spherical wind model can fit the time averaged light curve as measured by the RXTE ASM, but does not fit the observed changes in the absorption column or account for the existence of the phase-locked secondary flare. An additional model component consisting of a trailing stream can account for the variations in column depth. However, these models favor a high inclination angle for the system, suggesting a companion mass more consistent with an identification as a Be-star. In this case an equatorially enhanced wind and inclined neutron star orbit may be a more appropriate interpretation of the data.

1. Introduction

4U1907+09 was noted as a variable X-ray source during the early sky surveys with Uhuru (Giacconi et al. 1971), Ariel V (Seward et al. 1976), OSO-7 (Markert et al. 1978), and HEAO-1 (Schwartz et al. 1980). The latter allowed Schwartz et al. (1980) to identify the source with a heavily reddened $m_v \simeq 16.4$ star having a broad H_α emission line, which they assumed was an OB supergiant. A large X-ray outburst observed by Ariel V during January 1980 indicated regular flux modulation on a time scale of days. Further analysis of all the Ariel V data revealed a period of 8.4 days (Marshall and Ricketts 1980). The folded period profile shows a large primary peak as well as a smaller secondary maximum \sim half a cycle later. Long term observations by Vela 5B seemed to indicate an additional quasi-periodicity at $P \sim 41.6$ days, which was proposed to be due to precession similar to that of Her X-1 (Priedhorsky and Terrell 1984).

In 1983, Tenma observed 4U1907+09 for an entire 8 day cycle, which resulted in the discovery of double peaked 437.5 s pulsations (Makishima et al. 1984). Analysis of the pulse arrival times allowed an estimate of the orbital parameters to be made, which confirmed the 8.38 d period as the orbital period. A moderately eccentric ($e \sim 0.22$) orbit best fit the data, although a circular orbit also provided an adequate fit. Makishima et al. also determined a mass function of $\sim 9M_\odot$, confirming the massive nature of the companion. Further observations by EXOSAT (Cook and Page 1987) implied a mean spin-down rate

of $\sim 0.23 \text{ s yr}^{-1}$, a variable column density ($1.5 - 5.7 \times 10^{22} \text{ cm}^{-2}$), and slightly refined the Tenma orbital elements. The observed spectra were consistent with a hard power-law ($\alpha \sim 1.2$) with variable low-energy cut-off. Balloon observations of 4U1907+09 in the 20-100 keV range and analysis of Einstein archival data are consistent with the EXOSAT spectral observations (Chitnis et al. 1993).

Ginga spectral studies suggested a cyclotron absorption feature at $\sim 19 \text{ keV}$ (Mihara 1995; Makishima et al. 1999), which has been confirmed by a recent SAX observation (Cusumano et al. 1998), along with the discovery of the second harmonic at 39 keV, suggesting a surface magnetic field strength of $\sim 2 \times 10^{12} \text{ Gauss}$. An iron emission line at $\sim 6.4 \text{ keV}$ was also detected, with an equivalent width of $\sim 60 \text{ eV}$. A pulse period of $\sim 439.5 \pm 0.6 \text{ s}$ is clearly seen in the Ginga data during most of the observations where the source had an average intensity of 15-20 mCrab. However 4U1907+09 also exhibited extended periods of weaker intensity ($\sim 3 \text{ mCrab}$) accompanied by a reduced pulsed fraction (Makishima et al. 1999).

Iye (1986) performed the first detailed spectroscopic studies of the companion star to 4U1907+09. He concluded, in contrast to the initial assumptions by Schwartz et al. (1980) that the spectral type of the companion was B2 III – Ve, and that the two X-ray flares seen in some orbits were due to the intersection, and subsequent accretion of material in an extended disk around the companion by the orbiting neutron star.

van Kerkwijk, van Oijen, and van den Heuvel (1989) next undertook extensive spectroscopic studies to determine whether the companion to 4U1907+09 is an OB supergiant or a Be-star. They considered X-ray, optical and orbital data and suggested most of the measurements support the supergiant nature of the companion, including reddening

¹Current address: McGill University, Physics Department, 3600 University St., Montreal, Quebec, H3A 2T8

²Current address: Iowa State University c/o Smithsonian Institution, Steward Observatory 933 N. Cherry Ave., Tucson, AZ 85719

ing and distance, H_α FWHM, and rotation velocity of the companion. In addition, the location of 4U1907+09 in the spin-period versus orbital-period diagram (Corbet 1984) is inconsistent with the trend observed for most Be/X-ray pulsars, suggesting instead a wind-fed supergiant system. Since it is difficult to produce a phase-locked secondary flare from the wind of a supergiant star, van Kerkwijk, van Oijen, and van den Heuvel (1989) suggested the secondary flare may be spurious in nature. There is one clear case of a wind-fed supergiant/X-ray pulsar system, GX 301-2, which has a tendency to flare twice per orbit for extended periods of time (Pravdo et al. 1995), but the cause of this is not well understood.

Recent observations of 4U1907+09 with RXTE showed highly variable flux with frequent drops to below the detection threshold (in't Zand, Strohmayer and Baykal 1997). There is no evidence for increased absorption during the drops in their data, suggesting the low flux levels are due to a low accretion rate. A possible flare that is consistent in phase with previously observed secondary flares was also seen in the RXTE data. The 2-30 keV RXTE spectrum is well fit by a cutoff power-law having a photon index $\alpha \sim 1.0 - 1.3$ with a cutoff energy of 13.6 keV, and N_H varying from $1-9 \times 10^{22} \text{ cm}^{-2}$, the lowest values occurring during the secondary flare. No evidence for line emission was found with $\sim 60 \text{ eV}$ upper limit on an iron line equivalent width.

By combining the RXTE data with the Tenma data, in't Zand, Baykal, and Strohmayer (1998) obtained a slightly improved orbital fit. This allowed a good determination of the orbital period (8.3753 ± 0.0003 days). However, the eccentricity is still not well determined, with a 68% confidence region of 0.14-0.38. They also reported the discovery of 18 s oscillations during a 1 hr flare, which may be the result of the beat frequency between the spin

period and an accretion disk. In addition, the measured spin period $P_s = 440.341_{-0.017}^{+0.012}$ suggests the pulsar has been steadily spinning down since 1983, with $\dot{P}_s = +0.225 \text{ s yr}^{-1}$.

In this paper we present timing and spectral analysis of four ASCA observations of 4U1907+09 and spectral analysis of an additional 9 RXTE observations, roughly equally spaced around the 8.4 day orbit. We also report on archival observations of this source with HEAO A-1 and the RXTE All Sky Monitor. We then compare these and all previous observations of 4U1907+09 to a model of accretion from a spherical wind coming from the companion.

2. Archival Observations

We have investigated archival HEAO A-1 scanning data on 4U1907+09. HEAO A-1 observed 4U1907+09 in a series of 32 s scans during 1978 April 7 - 14. The data show orbital behavior consistent with the Tenma/EXOSAT period with two peaks at orbital phases consistent with what was seen by Ariel V. The lightcurve from the A-1 observations is shown in Figure 1.

The RXTE All Sky Monitor has been observing this source since it began regular observations in February, 1996. We report here on ~ 1400 days of data (MJD 50136-51549). Errors on individual flux measurements are relatively large, making examinations on time scales of days unreliable. However, epoch folding of the light curve clearly shows the orbital modulation. In Figure 2 we show the average orbital light curve for the entire data set, with the orbital period and epoch $T_{\pi/2}$ from in't Zand, Baykal, and Strohmayer (1998). The vertical lines represent the 68% confidence region of the time of periastron. There is evidence for a secondary flare at a phase of ~ 0.15 . We also folded separately the light curves from the 3 energy channels (1.3-3.0

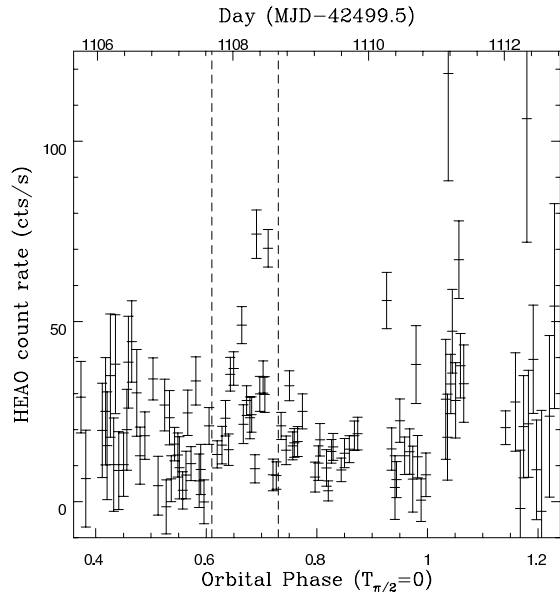


Fig. 1.— Light curve of 4U1907+09 during the 1978 HEAO A-1 observations. The vertical lines in this and the following figures represent the 68% confidence region of the time of periastron.

keV, 3.0-5.0 keV, and 5.0-12.1 keV) of the ASM and found evidence for the secondary flare at a consistent phase in each. A comparison of the first half of the data set to the second showed this is a fairly stable feature. The ratio of the flare to quiescent flux is difficult to estimate since there is known to be a positive flux bias in the ASM data. In the case of 4U1907+09 this bias is exacerbated by several nearby sources including GRS 1915+105 and W49B.

We have also performed a period search on the ASM data in order to search for other periodicities such as the proposed 41 day periodicity (Priedhorsky and Terrell 1984). We binned the data into 20 phase bins and calculated χ^2_{ν} for a constant model averaging over phase, as recommended by Collura et al. (1989). As Figure 3 shows, the 8.375 day orbital period and several multiples of

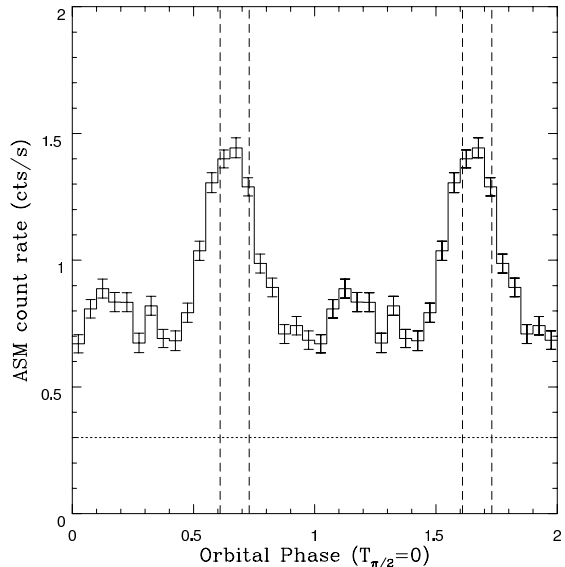


Fig. 2.— RXTE All Sky Monitor light curve of the 8.3753 day orbital period averaged over the 4 year data set. The dotted line is the level of positive flux bias assumed for later model fits.

it are poorly fit by a constant model. Although not evident in the ASM data folding, five times the orbital period would correspond to 41.9 days which is consistent with the quasi-periodicity seen in the *Vela 5B* data by Priedhorsky and Terrell (1984) and interpreted as an additional, longer period. We find no evidence for a periodicity in the long-term light-curve of this system which is unrelated to the orbital period.

3. ASCA Observations

In August 1996, ASCA made four 10 ks observations of 4U1907+09, roughly equally spaced throughout the 8.4 d orbit. Observational parameters are listed in Table 1. Extraction regions of 6' radius were used for the GIS detectors, while a 4' radius was used for SIS0. A slightly smaller region was used for SIS1 ($\sim 3.5'$) since the source was nearer the edge of the chip. Since the source is in the

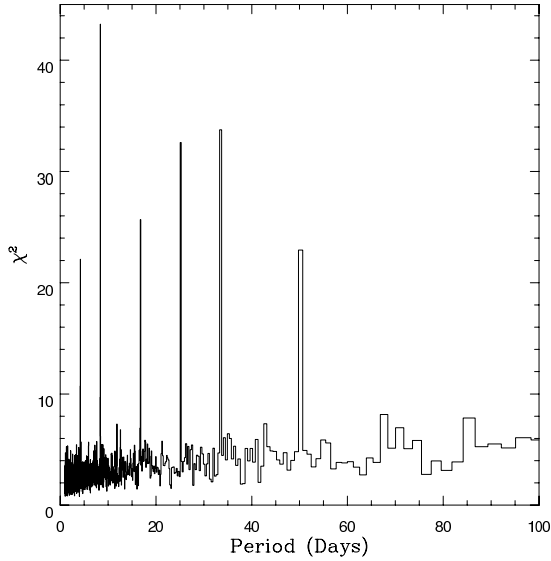


Fig. 3.— Period search of the RXTE All Sky Monitor data showing the 8.4 day orbital period and multiples.

galactic ridge a local estimate of the background is necessary. Therefore, source free regions of the detectors were used for extracting background light curves and spectra with a background rate of $\sim 3 \times 10^{-2}$ cts/s in each detector.

3.1. Temporal Analysis

The background subtracted GIS3 light curve for all 4 observations (Aobs1-4) is shown in Figure 4. Aobs1 consists of short flaring episodes with times of low flux in between where the count rate dropped by a factor of ~ 10 , reminiscent of the “dipping” seen in the earlier RXTE observations (in’t Zand, Strohmayer and Baykal 1997). Aobs2 and Aobs3 show the source in a very low state, a factor of ~ 50 below the average flux in Aobs4 and about a factor of ~ 4 below the low flux states in Aobs1. Since Aobs4 has the best statistics and is relatively constant on time scales longer than the pulse period, we used it to find the best pulse period of 440.35 ± 0.06

sec (after correcting the arrival times for the orbital motion of the pulsar, assuming the orbital parameters of in’t Zand, Baykal, and Strohmayer (1998)) by epoch folding the light curve. We then folded each of the observations at this period and show these in Figure 5. The pulses seem to change shape and become weaker during the low states (Aobs2 and Aobs3).

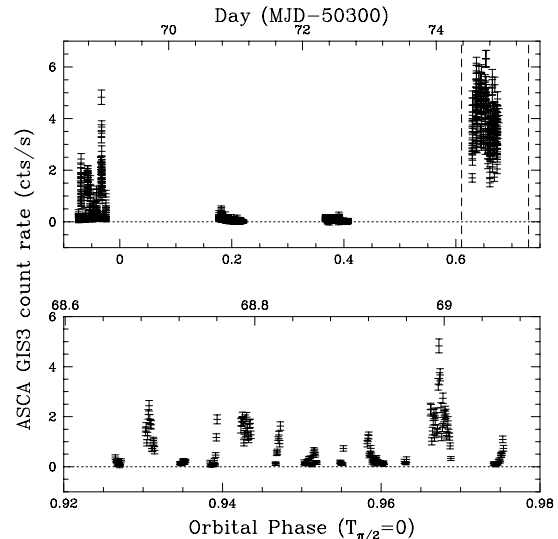


Fig. 4.— The ASCA GIS light curve of the four observations of 4U1907+09 (upper panel) and of just Aobs1 (lower panel).

3.2. Orbital Phase Spectroscopy

Using Xselect, spectra were extracted from each of the four detectors for each observation. These were analyzed using XSPEC and fit to an absorbed power law model, adding narrow ($\sigma = 0$) Gaussian lines if they significantly improved the fit. Aobs2 and Aobs3 had very low statistics so the two GIS detectors were combined into one data set, as were the two from the SIS detectors. In order to use all available photons, SIS Bright mode data were used. The results are shown in Table 2. It can immediately be seen that

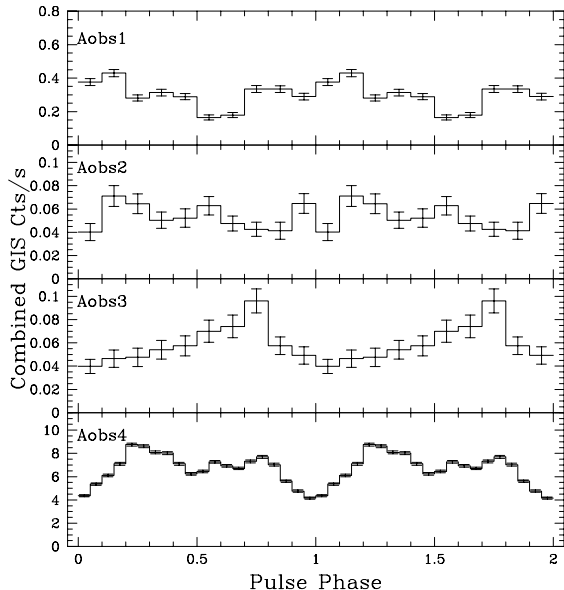


Fig. 5.— Pulse profiles from the ASCA observations. The photon arrival times are corrected for the pulsar orbit, and folded from a common epoch using the best fit period of 440.35s from epoch folding obs4. The error in the period results in a relative phase uncertainty between obs1 and obs4 of ~ 0.15 .

the lower states (Aobs2 and Aobs3) show no evidence of increased absorption. The lowest absorption occurs during Aobs4, the brightest observation, and is a factor of 2 lower than the high absorption seen during Aobs1. The spectral slope changes by a small, but statistically significant, amount. Weak iron line emission is present during Aobs4 and may be present during the other observations, although the statistics were not good enough to give more than upper limits at the 90% confidence level.

In order to test whether the drops in flux during Aobs1 are due to an increase of column depth, we extracted spectra separately from the flaring and the low portions of the data set. As shown in Figure 6, there is no evidence of increased absorption during dips. In fact, there is evidence that the absorption

column *decreases* during the dips, although the statistics on the low flux are such that the data are barely consistent within the 90% multi-parameter confidence region. There is no evidence of a significant change in photon index. If we assume the photon index remains constant, the change in absorption column is $\sim 2 \times 10^{22} \text{cm}^{-2}$. In the SIS data during the periods of low flux there appears to be an emission feature near 3.8 keV, which is evident in both SIS0 and SIS1, although not apparent in the GIS data. In the GIS data the fit could be significantly improved by an inclusion of a 0 width Gaussian line at 2.2 keV. This feature appears in several of the data sets, although since it is near the known bump in the response due to Gold in the telescopes, this feature should be viewed with caution.

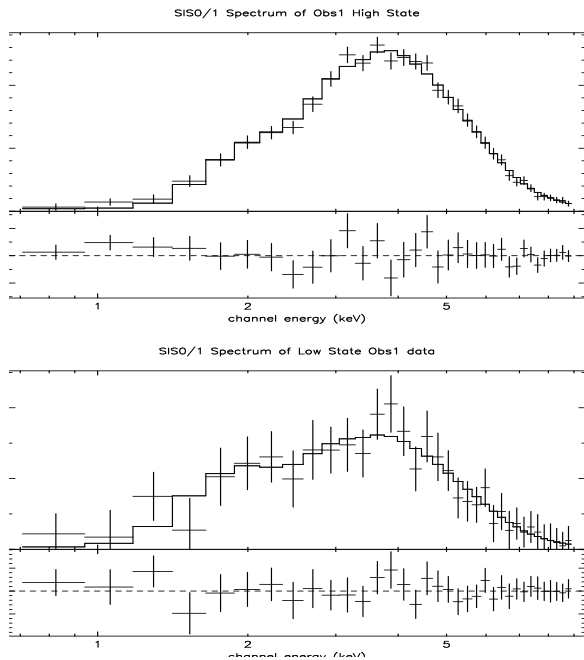


Fig. 6.— High state and low state SIS energy spectra for Aobs1.

During Aobs4 the source was only varying by a factor of 2 or so, mostly due to the pulsations, and had a fairly high count rate allowing tight constraints on N_H and the photon

index. The fits are significantly improved by the inclusion of an iron line at ~ 6.4 keV. The count rates were sufficiently high during this observation to extract spectra as a function of pulse phase using the best fit pulse period. There is no strong evidence for variability in N_H . A strong anti-correlation between photon index and intensity is evident which we show in Figure 7. There also seems to be a concentration of iron line emission in the pulse phase 0-0.1 spectrum. However, the uncertainties in the fit line strength at the other phases preclude a definitive measurement of line strength variability.

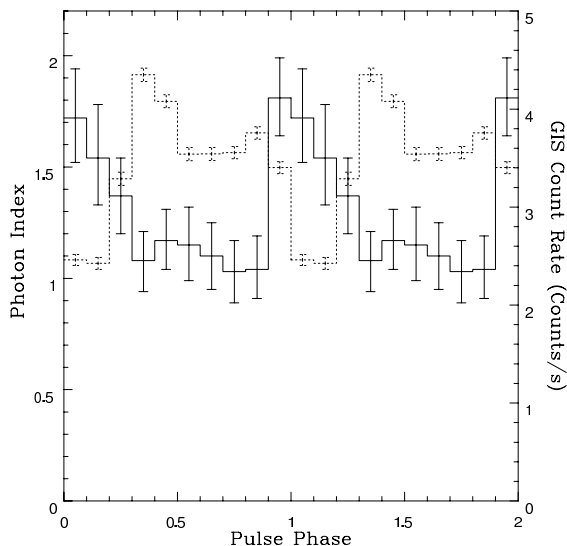


Fig. 7.— The photon spectral index as a function of pulse phase (arbitrary epoch) during Aobs4. Errors represent the 90% confidence region. The dotted histogram is the GIS count rate.

4. RXTE Observations

RXTE observed 4U1907+09 for a second series of observations during December 1996. A total of 9 observations (Robs1-9), each approximately 2 ksec in duration, were made spaced roughly one day apart in order to

evenly sample the 8.4 day orbit. Data from the Standard2 observational mode were analyzed using FTOOLS 4.2. Combined spectra were extracted from all 5 PCUs (except obs1, which only had PCUs 0-3 on during the observation) and all layers. Model background spectra were then constructed using the background models provided by the RXTE Science Operations Facility, which take into account the particle induced background. However, they do not take into account the X-ray background from the galactic plane. To construct an accurate background model for 4U1907+09, it is necessary to take into account contributions from both the Galactic ridge and the nearby supernova remnant W49B. During two of the observations, Robs4 and Robs5, the source was in the “dip” state. The model background was subtracted from these observations, and their spectra were examined. The count rate of ~ 18 cts/s is comparable to what is observed by RXTE for the diffuse emission from the Galactic ridge (Valinia and Marshall 1998). We created a crude model of the Galactic ridge plus SNR W49B emission consisting of two thermal bremsstrahlung sources with fixed temperatures of 1.8keV and ~ 10 keV, moderate ($1.6 \times 10^{22} \text{cm}^{-2}$) absorption, and a ~ 6.7 keV gaussian lines with only the normalizations allowed to vary. These parameter values were taken from Koyama (1989) for this position in the galactic ridge and Smith et al. (1985) for W49B. This model adequately fit the data for Robs4 and Robs5 with normalizations that could reasonably be expected if the source had dropped to flux levels consistent with the low states seen in the ASCA data and the spectra were dominated by emission from the Galactic ridge and the nearby thermal supernova remnant. Therefore, these observations were used to make a background spectrum for use in spectral fits of the other observations in the following way. Using the background

models available from the RXTE GOF, we generated background spectra for all 9 observations. These were directly subtracted from the observation spectra using the `mathpha` FTOOL to create the files to be used in the fitting. The background subtracted `pha` files of `Rob4` and `Rob5` were then added together to create a local X-ray background for 4U1907+09 which was used as the background file in XSPEC.

All the spectra from the remaining seven observations were modelled using an absorbed power-law with a high-energy cutoff in XSPEC. The data were fit in the energy range of 2.5 - 20 keV, and the results are listed in Table 4. The measured cut-offs are consistent with the broad-band spectral fits of Beppo-Sax (Cusumano et al. 1998). We also obtained the archival RXTE data from February 1996 first analyzed by in't Zand, Strohmayer and Baykal (1997) to fit for average fluxes and absorption in the 2.5-10 keV band for inclusion in the modelling below.

5. Modelling of Orbital Spectral Variations

In Figure 8 we show measurements of nH as a function of orbital phase for spectral measurements from ASCA and RXTE (this work), EXOSAT (Cook and Page 1987), Tenma (Makishima et al. 1984), and SAX (Cusumano et al. 1998). As a consistency check, we also plot the ASM hardness ratio of (5.0-12.1 keV cts/s)/(1.3-3.0 keV cts/s) as a function of phase (dotted line). Since the spectral slope does not vary greatly, we expect this hardness ratio to change mostly due to column depth. The vertical lines represent the 68% confidence region of the time of periastron. We see that the absorption begins to increase towards the end of the primary flare stays high until right before the secondary flare, where it drops again. In Figure 9 we plot the photon spectral index as a function

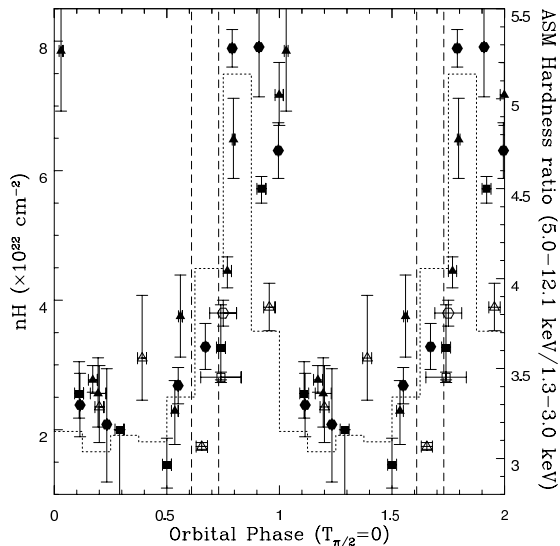


Fig. 8.— The multi-mission measurement of nH as a function of orbital phase. Measurements are from ASCA (open triangles), Feb. 1996 RXTE (filled triangles), SAX (open square), EXOSAT (filled square), Tenma (open hex), and Dec. 1996 RXTE (filled hex). The histogram is the ASM hardness ratio of the countrates from channel 3 over channel 1.

of orbital phase. Small but significant changes are observed. In Figure 10 we plot the 2-10 keV flux measurements from these same observations versus orbital phase with the ASM lightcurve overplotted. The secondary flare is twice seen to be nearly as bright as the primary during these observations. One of the RXTE observations seen at an overlapping phase with the ASCA Aobs2 is still seen to be moderately bright ($F_X \sim 10^{-10}$ ergs $\text{cm}^{-2} \text{s}^{-1}$) although dipping activity is seen during the observation. Therefore, extended periods of low flux as seen in the ASCA Aobs2 and Aobs3 probably do not occur every orbit. In general there is a positive flux bias of ~ 0.1 cts/s in ASM data. However, in crowded regions of the Galactic plane, such as around 4U1907+09, there are likely to be further systematic biases. By comparing the

folded ASM light curve to the observed multi-mission fluxes we estimate a positive flux bias of $\sim 0.2 - 0.6$ cts/s. We will assume a bias of 0.3 for the analysis below.

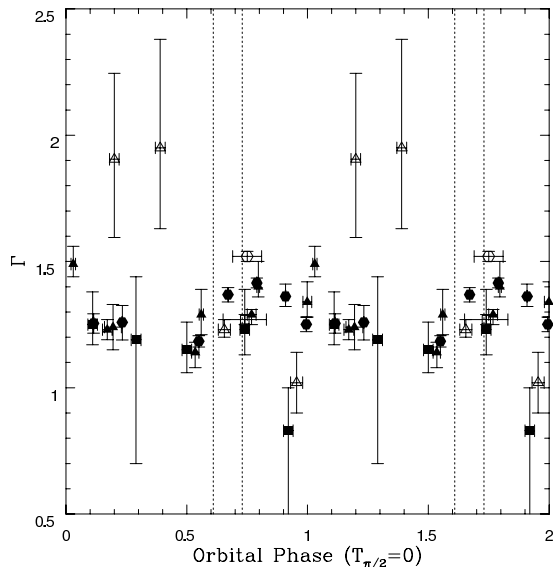


Fig. 9.— The multi-mission measurement of the photon index as a function of orbital phase.

In this section we model the primary flare and absorption as accretion from a spherical stellar wind with the addition of an absorbing gas stream. This model, first applied to Tenma observations of GX 301-2, is detailed in Leahy (1991). We first attempt to model the average ASM lightcurve and multi-mission absorption data as accretion from a simple spherical stellar wind with velocity profile:

$$v_{wind} = v_{\infty}(1 - R_c/r)^{\beta}$$

where v_{∞} is the terminal velocity, assumed to be 3 times the escape velocity, and R_c is the radius of the companion. The Castor, Abbott, and Klein (1975) theoretical wind model has $\beta = 0.5$, but observations of OB stars (Leitherer 1988; Boroson et al. 1999) suggest that $\beta \sim 0.7 - 2$ depending on spectral type.

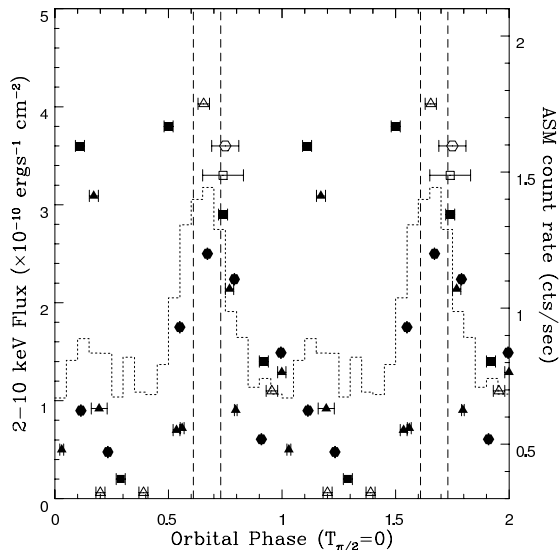


Fig. 10.— The multi-mission measurement of the 2-10 keV flux as a function of orbital phase. The histogram is the folded lightcurve from the ASM, with the y axis starting at the assumed flux bias of 0.3 cts/sec.

We assume $\beta = 1$, consistent with the assumption of an OB supergiant. In the case of a lower mass Be-type star, models of the wind structure are more complex and uncertain. However, the velocity profile of the polar wind from a Be-star is similar to that of an OB supergiant (de Araújo, de Freitas Pacheco, and Petrini 1994), and the profile of the equatorial wind probably has a similar functional form but lower terminal velocity. If the companion is a Be-star, it is likely that the spin axis is not aligned with the orbital axis (see discussion) and so emission dominated by accretion from the polar wind over much of the orbit may not be an unreasonable assumption.

We assume the orbital period $P = 8.3753d$, longitude of periastron (i.e. the observer's viewing angle) $\omega = 330$ deg, and periastron phase of the best fit model from in't Zand, Baykal, and Strohmayer (1998) and fit the ASM light curve for a range of inclination an-

gles by adjusting the eccentricity and the parameter $x = \dot{M}_{20}/d_3^2$, where \dot{M}_{20} is the mass loss rate in units of 10^{20} grams/sec and d_3 is the distance in units of 3 kpc. We choose as our canonical values $i = 47.9$, which implies a companion mass $M_c = 24M_\odot$ given the mass function derived from the orbital fits assuming a neutron star mass of $1.4M_\odot$, and $i = 75.7^\circ$ for a companion mass $M_c = 12M_\odot$ more in line with a Be-star.

For the companion radius we follow van Kerkwijk, van Oijen, and van den Heuvel (1989) and assume $R_c = 31R_\odot$ for a $24M_\odot$ star. However, a star of this radius would be larger than its Roche lobe at periastron, as defined in Brown and Boyle (1984), assuming the best fit eccentricity of $e = 0.28$ (in't Zand, Baykal, and Strohmayer 1998), a rotational velocity $v_{\text{sin}i} = 90$ km/s (van Kerkwijk, van Oijen, and van den Heuvel 1989), and alignment of the rotational and orbital axes. In Figure 11 we plot the Roche lobe radius as a function of companion mass as well as the limits on radius inferred from the lack of eclipses. All supergiant companions would greatly overflow their Roche lobes and would have to be excluded if we assume this as a radius limit. However, a non-rotating (or non-aligned) star has a greater Roche lobe radius, as would a system where the eccentricity is less. For the $12M_\odot$ star, we use the Iye (1986) value of $R_c = 6R_\odot$ for a Be-star companion. For intermediate inclinations and masses, the appropriate radius is dependent on spectral type. For supergiants, the radius actually increases with decreased mass, which would exacerbate the Roche lobe problem. However, a type Ib, III, or V are all smaller than our canonical Ia supergiant star. In Figure 11 we plot radii for a number of early B stars (Underhill and Doazan 1982). A linearly interpolation between our two canonical stars seems to provide a reasonable mass-radius relationship for modelling purposes.

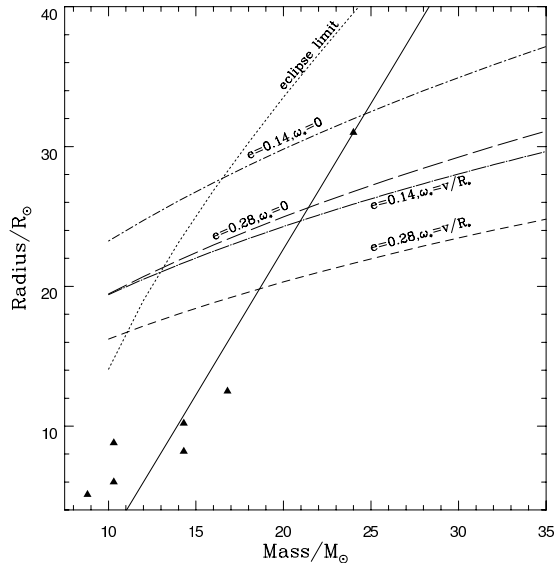


Fig. 11.— Assumed Mass/Radius relationship (solid line) compared to eclipse limit and periastron “Roche Lobe” radii assuming different eccentricities and stellar rotation rates in the orbital plane (Ω_*). Points are various stellar values for main sequence, giant, and supergiant B0-B3 stars (Underhill and Doazan 1982)

In Figure 12 we show the range of model curves compared to the ASM light curve. To fit the higher mass companion to the shape of the primary flare an eccentricity $e \lesssim 0.14$ is required (which would also allow the star to underfill its Roche lobe at periastron). For the lower mass companion the best fit to the observed primary flare peak is $e = 0.26$, more in line with the best fit eccentricity from the pulse arrival analysis. In no case can a secondary flare be produced from this model.

This luminosity model implies a varying absorption as a function of orbital phase, with the overall normalization being only a function of \dot{M} . Using the parameters given above and an assumed interstellar absorption of $nH = 1.5 \times 10^{22} \text{cm}^{-2}$, we find that $\dot{M}_{20} = 1 - 1.5$ best fit the absorption data over

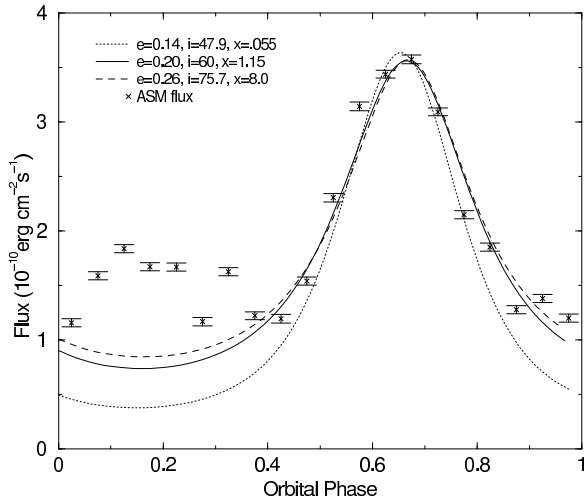


Fig. 12.— Spherical wind model fits to ASM lightcurve assuming inclination angles of 47.9° ($M_c = 24M_\odot$), 60° ($M_c = 16M_\odot$), and 75.7° ($M_c = 12M_\odot$).

our range of inclination angles. This is somewhat low for a B supergiant, but quite high for a Be-star (de Araújo, de Freitas Pacheco, and Petrini 1994). In order to improve the fit, we also vary the the longitude of periastron since that is poorly constrained by the pulse arrival time analysis of in’t Zand, Baykal, and Strohmayer (1998). In Figure 13 we plot the results compared to the multi-mission data. Neither the phase or the amplitude of the large increase in absorption after periastron can be produced from this simple spherical wind model.

We can use the \dot{M} from the absorption fits and the parameter x from the luminosity model to estimate distances to the system. For the $24M_\odot$ model, we derive a distance $d \sim 4.3$ kpc, while for the $16M_\odot$ and $12M_\odot$ models, we derive $d \sim 1.0$ kpc and $d \sim 0.4$ kpc respectively. The first is in line with the distance estimates of 5.9 to 2.4 kpc for a supergiant companion from van Kerkwijk, van Oijen, and van den Heuvel (1989), and the latter are consistent with their estimates of

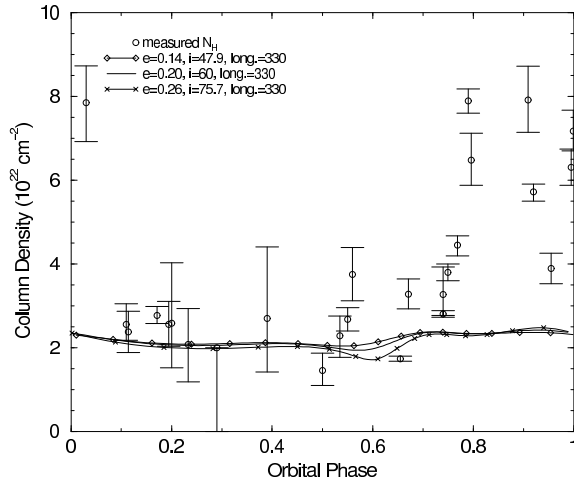


Fig. 13.— Spherical wind model absorption compared with multi-mission spectral fits.

1.5 to 0.6 kpc for a giant. Note that the minimum measured $nH \sim 1.5 \times 10^{22} \text{cm}^{-2}$ means the assumed interstellar component of the absorption is an upper limit. Thus the derived values of \dot{M} , and hence the inferred distances, should be considered lower limits.

To fit the post-periastron absorption, we added a linear trailing gas stream to the above model (see Leahy (1991) for details). Such a stream can be interpreted as arising from the wake caused by the passage of the neutron star through the wind, or from an accretion stream coming from the companion (although this latter interpretation would require modification of the luminosity model). The stream is modelled as a density enhancement with a gaussian profile perpendicular to the stream line, an exponential cutoff on the front side and no cutoff in the downstream direction. The total contribution to the absorption is then obtained by integrating along the line of site. For a given orbital phase, longitude of periastron, and orbital inclination, the amplitude of the absorption enhancement of the trailing gas stream is completely determined by the product $n_o \sigma \sim 10^{22} \text{cm}^{-2}$, where n_o is the central density and σ the gaussian width.

The additional absorption due to the stream is shown in the top of Figure 14. The phase of the absorption peak is somewhat earlier than indicated by the data, so we also tried offsetting the stream line towards the companion star by angles of 20° and 40° . The bottom panel of Figure 14 shows how the combined wind plus stream model compares to the absorption data for the various cases. We find that an adequate fit can be obtained with the larger inclination angles and an offset stream. A downstream cutoff of the stream would tend to broaden the peak somewhat, which might further improve the fit.

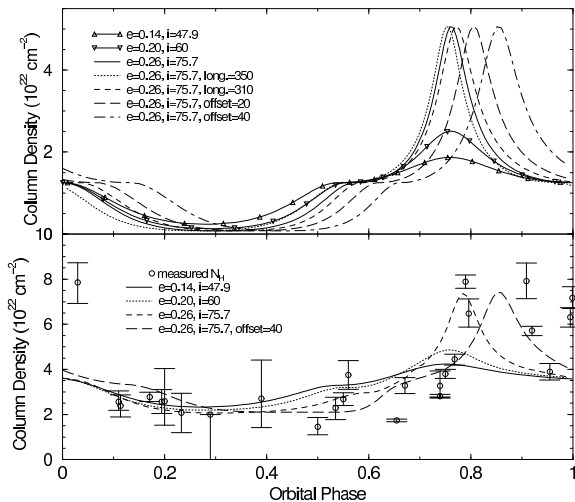


Fig. 14.— Absorption due to a trailing gas stream. The top panel shows the orbital variation of absorption due to the stream for various parameters. The bottom panel shows the wind plus stream absorption model compared to the multi-mission measurements of nH.

6. Discussion

If the eccentricity of $e \gtrsim 0.2$ of the best fit orbital parameters from pulse arrival time analyses is correct, the primary flare seen in the overall light curve can be fit using a model of accretion from a spherical wind off of a star of mass $M_c \lesssim 16M_\odot$. However, the absorp-

tion measurements and the persistence of the secondary flare require modifications to this model. We have shown that a trailing accretion stream moderately offset towards the companion can account for the extra absorption component, although not the secondary flare. Such an offset stream may be indicated by the high resolution two-dimensional hydrodynamical simulations of Benensohn, Lamb, and Taam (1991). The “flip-flop” instability seen in their simulations modifies the direction of the downstream flow so that it switches back and forth resulting in a wake that could be characterized by two offset streams, one of which could provide the enhanced absorption seen in the data (see Fig. 2 of Benensohn, Lamb, and Taam (1991)). This instability can in principle also explain the “dipping” or “flaring” behavior seen in Aobs1 and in the RXTE observations of in’t Zand, Strohmayer and Baykal (1997), and may even be compatible with a drop in absorption during low accretion phases. However, this instability may just be an artifact of two-dimensional simulations, and whether similar affects occur in a three-dimensional flow is an open question. Recent 3D simulations by Ruffert (1999) do exhibit active unstable phases, although the changes in accretion rate tend to be smaller and the downstream density profile is unclear.

The spherical wind accretion models favor a high inclination angle, implying a companion mass more in line with a Be-star than a supergiant. In addition, if the companion mass is high, the models imply an eccentricity near the low end of the acceptable range. This lower eccentricity is also required to keep a massive supergiant from greatly overflowing its Roche lobe near periastron. Even with a smaller eccentricity, it is likely that periodic Roche lobe overflow (Brown and Boyle 1984) or tidal stripping (Layton et al. 1997) would be the dominant mass transfer mechanism. In this case, the observed accretion rate

and orbital variation may be somewhat low, unless long-term storage of material by an accretion disk could keep the accretion rate low except for occasional large outbursts like the one seen by Ariel V in 1980 (Marshall and Ricketts 1980). If the best fit eccentricity value of $e \sim 0.28$ is correct, it would seem to exclude the accretion from a supergiant wind model. This suggests that an alternative model of the accretion perhaps should be considered. One persistent possibility is an equatorially enhanced wind with the neutron star in an inclined orbit, as suggested by Iye(1986). In this case, the neutron star passes behind an extended matter disk around the companion after periastron and comes back through after apastron. While tidal forces would tend to align the neutron star orbital axis with that of the companion’s spin axis, the timescale for this is similar to the circularization timescale, and accretion processes might counteract the tidal forces somewhat (Matese and Whitmire 1983). Given that the orbit is eccentric, we do not view a somewhat inclined orbital axis as being unreasonable.

In the equatorially enhanced wind scenario, the flares are fed by matter gathered by the neutron star as it passes through the matter envelope. If the outflow speed is somewhat slower near the equator, the size of this envelope might be limited by the neutron star’s orbit. Such truncation is indicated from studies of the $H\alpha$ emission line in several Be/X-ray binary systems (Zamanov et al. 2000). The matter is depleted by the periastron passage of the neutron star, so significantly less material is available further out at the apastron radius. If sufficiently depleted, there may be no secondary flare at all. Hence we get an intermittent but phase locked secondary flare.

The major difficulty to this picture is the “virtually certain” classification of the companion as a supergiant by van Kerkwijk, van Oijen, and van den Heuvel (1989). This is

based on a collection of observed properties of the system, with some favoring a Be-star, and some favoring a supergiant. Two factors seem to greatly favor the supergiant interpretation. First is the color excess $E_{B-V} = 3.4 \pm 0.2$, which is quite high for the inferred distance of $\lesssim 1.5$ kpc of a Be-star. However, the variation in absorption column with orbital phase suggests that much of this could be local. Indeed, the average excess determined from interstellar absorption lines is only $E_{B-V} = 2.4 \pm 0.5$ or $E_{B-V} = 2.7 \pm 0.6$, depending on which coefficients for the ratio of equivalent width to color excess used (van Kerkwijk, van Oijen, and van den Heuvel 1989). These lower values are more in line with the inferred interstellar X-ray absorption of $nH \lesssim 1.5 \times 10^{22} \text{cm}^{-2}$. The independent distance estimate van Kerkwijk, van Oijen, and van den Heuvel (1989) obtain from the interstellar sodium lines of $d = 2.1 \pm 0.6$ is between the supergiant and Be-star distances, and consistent with both given the error.

The second factor strongly favoring the supergiant interpretation is the large FWHM ~ 700 km/s of the $H\alpha$ line combined with the relatively low projected rotational velocity $v_{\text{sin}i} \sim 90$ km/s. While neither value is exceptionally unusual for a Be-star, the combination is (Dachs et al. 1986). The inclination angle suggested by the observed projected rotational velocity is $i \sim 15^\circ$ assuming typical Be-star rotational velocities, as opposed to the inferred orbital inclination $i \sim 60^\circ - 75^\circ$ of the neutron star with a giant or main sequence star companion, consistent with the inclined orbit scenario. However, the large value of the FWHM suggests the outflowing disk is seen nearly edge on. The circumstellar envelope can and would be affected by the neutron star, as evidenced by the large-scale perturbations observed in the $H\alpha$ profiles of several Be/X-ray binaries (Negueruela et al. 1998). Since the orbital period of 4U1907+09

is shorter than any of the known Be/X-ray binaries (except A0538-66, which is not well observed), it would be expected to have a much greater perturbing effect. It is interesting to note that the projected orbital velocity of a particle in the orbital plane near the Roche lobe radius of a lower mass star in 4U1907+09 is roughly half the observed $H\alpha$ FWHM. If the gravitational attraction of the neutron star could warp the equatorial outflow of the companion such that it would be nearly co-planar to the neutron star orbit at the Roche lobe radius, the observed FWHM might result. Hydrodynamical simulations should be able to determine if such a scenario is feasible.

The relatively long periods of low accretion rate seen in Aobs2 and Aobs3 are somewhat puzzling. Inhomogeneities in the wind from the companion could possibly account for these variations, although the apparent duration of several days during the ASCA observations would argue against this. If the accretion is modified by a transient accretion disk, instabilities in the accretion disk could account for both the sudden changes in accretion rate seen in Aobs1 and the longer periods of quiescence seen in Aobs2 and Aobs3. The consistent spin-up of the neutron star and the 18 sec. oscillations seen by RXTE (in't Zand, Strohmayer and Baykal 1997) argue for the existence of an accretion disk. The on-off behavior seen by both RXTE and ASCA are suggestive of magnetically inhibited accretion from a disk whose inner edge is near the corotation radius. The residual emission during the off periods may then be a result of accretion on to the magnetosphere or a bow shock. However, the slow spin period and correspondingly large corotation radius makes this unlikely.

7. Comparison with GX301-2

4U1907+09 is similar in many respects to the wind fed Supergiant/X-ray pulsar binary system GX301-2. Both have eccentric orbits and occupy a similar location on the spin-period versus orbital-period diagram (Corbet 1986) (for GX 301-2, $e \sim 0.47$, $P_{spin} \sim 680s$, $P_{orb} \sim 41.5d$, Koh et al. (1997)). The absorption profile and primary orbital flux peak of both systems have been successfully fit by a spherical wind plus gas stream model (Leahy 1991). GX 301-2 also has extended periods where there is a secondary orbital flare at a consistent phase that cannot be fit by wind models. An equatorially enhanced outflow has also been suggested for this system and models of such an outflow can grossly fit the orbital light curve (Koh et al. 1997). Both systems have companions with similar temperatures (spectral type B2) and projected rotational velocities ($v \sin i \sim 70$ for GX 301-2, Parkes et al. (1980)).

However, the companion star of GX 301-2, Wray 977, is unambiguously identified as a supergiant by the strength of various lines in the blue portion of the spectrum (Parkes et al. 1980). The observations of Iye (1986) and van Kerkwijk, van Oijen, and van den Heuvel (1989) did not extend into the blue portion of the spectrum, so such diagnostics are not available for 4U 1907+09. The $H\beta$ emission line of Wray 977 has a P-Cygni profile (Parkes et al. 1980), clear evidence of an expanding atmosphere. No such profiles have been seen in 4U 1907+09.

The local absorption column and iron line equivalent width of the X-ray spectrum of GX 301-2 are both more than an order of magnitude stronger than in 4U1907+09. This implies the mass loss from Wray 977 is much greater than from the companion of 4U1907+09, despite the similarity in the proposed spectral classes. While enhanced mass

loss in these systems could be expected due to gravitational interaction with a neutron star, the orbit of GX 301-2 is significantly wider, and there is no question that the companion remains inside its Roche lobe (although at periastron it can come close, Leahy (1991)). If both were supergiants, the naive expectation would be greater mass loss from the companion of 4U1907+09 due to transient Roche lobe overflow (Brown and Boyle 1984) or tidal stripping Layton et al. (1997).

The changes in spectral index with pulse phase of both systems show a softening of the spectrum near the pulse minimum in the 1-10 keV band (Saraswat et al. 1996; Leahy and Matsuoka 1990). The iron line equivalent width in GX 301-2 varies with pulse phase as well, with a peak near the pulse minimum. The possible iron line enhancement near the pulse minimum in the 4U1907+09 *ASCA* data, if real, would be consistent. These similarities in the phase-resolved spectra suggest the accretion columns are similar. This is not surprising, since the spin periods and surface magnetic field strengths (as inferred from their cyclotron absorption lines) are similar.

8. Conclusions

Observations of the variation of the spectra of 4U1907+07 with orbital phase are consistent with a simple spherical wind accreting onto the neutron star from an OB supergiant companion with excess absorption caused by a trailing accretion wake. However, the implied inclination angle for such a model suggests a relatively low mass ($\lesssim 16M_{\odot}$) for the companion. The excess of absorption column seen after periastron might also be interpreted as the neutron star passing through an equatorially enhanced matter envelope in an inclined orbit. Observations of the secondary flare near apastron by RXTE and HEAO A-1, as well as the average orbital light curve from the RXTE ASM, further support the hy-

pothesis that this flaring has been occurring at a consistent phase but with variable amplitude for 20 years. The measurements of the low states by *ASCA* suggest that the accretion rate can change by 1-2 orders of magnitude over a short time period, perhaps due to a transient accretion disk. The most critical components to a better understanding of this system are more secure measurements of the orbital eccentricity and periastron phase and improved optical measurements of the companion. A high resolution optical spectrum at shorter wavelengths and orbital radial velocity measurements could unambiguously determine the companion type.

We thank J. G. Jernigan for useful discussions as to the nature of the companion star in this system and the anonymous referee for pointing out the importance of the Roche lobe radius. All Sky Monitor results were provided by the ASM/RXTE teams at MIT and at the RXTE SOF and GOF at NASA's GSFC. This work was supported in part by NASA Guest Observer grants NAG 5-2948 and NAG 5-3332.

REFERENCES

- Benensohn, J. S., Lamb, D. Q., & Taam, R. E. 1997, *ApJ*, 478, 723
- Boroson, B., Kallman, T., McCray, R., Vrtilik, S. D., & Raymond, J. 1999, *ApJ*, 519, 191
- Brown, J.C. & Boyle, C.B. 1984, *A&A*, 141, 369
- Castor, J. I., Abbott, D. C., & Klein, R. I. 1975, *ApJ*, 195, 157
- Chitnis, V. R., Rao, A. R., Agrawal, P. C., & Manchanda, R. K. 1993, *A&A*, 268, 609
- Collura, A., Maggio, A., Sciortino, S., Serio,

- S., Vaiana, G. S., & Rosner, R. 1987, ApJ, 315, 340
- Cook, M. C., & Page, C.G. 1987, MNRAS, 225, 381
- Corbet, R. 1984, A&A, 141, 91
- Corbet, R. 1986, MNRAS, 220, 1047
- Cusumano, G., Di Salvo, T., Burderi, L., Orlandini, M., Piraino, S., Robba, N., & Santangelo, A. 1998, A&A, 338, L79
- Dachs, J., Hanuschik, R., Kaiser, D., & Rohe, D. 1986, A&A, 159, 276
- de Araújo, F.X., de Freitas Pacheco, J.A., & Petrini, D. 1994, MNRAS, 267, 501
- Giacconi, R., Kellogg, E. Gorenstein, P., Gursky, H. & Tananbaum, H. 1971, ApJ, 165, L27
- in't Zand, J. J. M., Baykal, A., & Strohmayer, T. E. 1998, ApJ, 496, 386
- in't Zand, J. J. M., Strohmayer, T. E., & Baykal, A. 1997, ApJ, 479, L47
- Iye, M. 1986, PASJ, 38, 463
- Koh, D.T., Bildsten, L., Chakrabarty, D., Nelson, R.W., Prince, T.A., Vaughan, B.A., Finger, M.H., Wilson, R.B., & Rubin, B.C. 1997, ApJ, 479, 933
- Koyama, K. 1989, PASJ, 41, 665
- Layton, J.T., Blondin, J.M., Owen, M.P., & Stevens, I.R. 1997, New Astron., 3, 111
- Leahy, D.A. 1991, MNRAS, 250, 310
- Leahy, D.A. & Matsuoka, M. 1990, ApJ, 355, 627
- Leitherer, C. 1988, ApJ, 326, 356
- Makishima, K., Kawai, N., Koyama, K., & Shibazaki, N. 1984, PASJ, 36, 679
- Makishima, K., Mihara, T., Nagase, F., & Tanaka, Y. 1999, ApJ, 525, 978
- Markert, T. H. et al. 1979, ApJS, 39, 573
- Marshall, N. & Ricketts, M. J. 1980, MNRAS, 193, 7P
- Matese, J. J. & Whitmire, D. P. 1983, ApJ, 266, 776
- Mihara, T. 1995, Ph. D. Thesis, Univ. of Tokyo
- Negueruela, I., Reig, P., Coe, M.J., & Fabregat, J. 1998, A&A, 336, 251
- Parkes, G.E., Mason, K.O., Murdin, P.G., & Culhane, J.L. 1980, MNRAS, 191, 547
- Pravdo, S.H., Day, C.S.R., Angelini, L., Harmon, B.A., Yoshida, A., & Saraawat, P. 1995, ApJ, 454, 872
- Priedhorsky, W. C. & Terrell, J. 1984, ApJ, 280, 661
- Ruffert, M. 1999, A&A, 346, 861
- Saraswat, P., Yoshida, A., Mihara, T., Kawai, N., Takeshima, T., Nagase, F., Makishima, K., Tashiro, M., Leahy, D.A., Pravdo, S., Day, C.S.R. & Angelini, L. 1996, ApJ, 463, 726
- Schwartz, D. A., Griffiths, R. E., Thorstensen, J. R., Charles, P. A. & Bowyer, S. 1980, AJ, 85, 549
- Seward, F. D., Page, C. G., Turner, M. J. L., & Pounds, K. A. 1976, MNRAS, 175, 39P
- Smith, A., Peacock, A., Jones, L.R. & Pye, J.P. 1985, ApJ, 296, 469
- Underhill, A.B. & Doazan, V. ed. *B stars With and Without Emission Lines* 1982, CNRS, Paris and NASA, Washington D.C. (SP-456)

Valinia, A. & Marshall, F.E. 1998, *ApJ*, 505,
134

van Kerkwijk, M. H., van Oijen, J. G. J., &
van den Heuvel, E. P. J. 1989, *A&A*, 209,
173

Zamanov, R.K., Reig, P., Martí, J., Coe, M.J.,
Fabregat, J., Tomov, N.A., & Valchev, T.
2000, *A&Aaccepted*, astro-ph/0012371

TABLE 1
ASCA OBSERVATION PARAMETERS

Observation	Sequence ID	Date MJD-50300	Orbital Phase $T_{\pi/2} = 0$	On-Time ks	Mean GIS rate Cts/s
Aobs 1	44020040	68.65-69.06	0.93-0.98	10.2	0.702 ± 0.008
Aobs 2	44020010	70.75-71.12	0.18-0.22	10.1	0.067 ± 0.005
Aobs 3	44020020	72.34-72.53	0.37-0.39	9.3	0.064 ± 0.005
Aobs 4	44020030	74.54-74.94	0.63-0.68	9.9	3.447 ± 0.015

TABLE 2
ASCA SPECTRAL FITS

Observation	n_H $\times 10^{22} \text{cm}^{-2}$	Γ	line E keV	line EqW eV	$F_{2-10keV}$ $\times 10^{-10} \text{ergs cm}^{-2} \text{s}^{-1}$	$\chi^2_{\nu}(\text{dof})$
Fits from GIS2 + GIS3						
Aobs 1	$3.89^{+0.37}_{-0.36}$	$1.02^{+0.12}_{-0.12}$	$6.53^{+0.32}_{-0.52}$	76 ± 33	1.11 ± 0.02	0.58(38)
Aobs1 hi	$4.18^{+0.41}_{-0.38}$	$1.05^{+0.13}_{-0.12}$	$6.45^{+0.31}_{-0.22}$	82 ± 33	1.73 ± 0.02	0.50(38)
Aobs1 lo	$2.12^{+1.68}_{-1.12}$	$0.92^{+0.67}_{-0.53}$			0.23 ± 0.02	0.24(40)
Aobs 2	$2.59^{+1.44}_{-1.07}$	$2.07^{+0.81}_{-0.65}$			0.066 ± 0.005	0.25(40)
Aobs 3	$2.70^{+1.71}_{-1.28}$	$1.93^{+0.88}_{-0.73}$			0.066 ± 0.005	0.19(40)
Aobs 4	$1.74^{+0.06}_{-0.06}$	$1.23^{+0.04}_{-0.03}$	$6.53^{+0.11}_{-0.11}$	79 ± 16	4.20 ± 0.02	1.71(38)
Fits from SIS0 + SIS1						
Aobs 1	$3.83^{+0.39}_{-0.36}$	$1.03^{+0.14}_{-0.14}$	6.34 (frozen)	< 57.1	0.87 ± 0.01	0.53(289)
Aobs1 hi	$4.01^{+0.42}_{-0.39}$	$1.04^{+0.14}_{-0.15}$	6.34 (frozen)	< 65.8	1.42 ± 0.02	0.51(289)
Aobs1 lo	$2.47^{+1.72}_{-1.20}$	$0.96^{+0.69}_{-0.60}$			0.18 ± 0.01	0.35(35)
Aobs 2	$2.50^{+1.28}_{-0.93}$	$1.89^{+0.78}_{-0.64}$			0.051 ± 0.003	0.30(28)
Aobs 3	$1.85^{+1.23}_{-0.84}$	$1.34^{+0.72}_{-0.59}$			0.063 ± 0.004	0.19(28)
Aobs 4	$1.87^{+0.05}_{-0.06}$	$1.35^{+0.04}_{-0.04}$	$6.34^{+0.08}_{-0.08}$	70.0 ± 15.8	3.49 ± 0.02	0.83(324)

TABLE 3
RXTE OBSERVATION PARAMETERS

Observation	Obs ID	Date MJD-50400	Orbital Phase $T_{\pi/2} = 0$	On-Time ks	Mean raw PCA rate Cts/s
Robs 1	10154-02-01	36.40-36.45	0.02	2.4	243
Robs 2	10154-02-02	37.39-37.42	0.14	2.4	238
Robs 3	10154-02-03	38.39-38.42	0.25	2.4	233
Robs 4	10154-02-04	39.39-39.42	0.37	2.4	181
Robs 5	10154-02-05	40.39-40.42	0.49	2.4	179
Robs 6	10154-02-06	41.05-41.08	0.57	2.5	291
Robs 7	10154-02-07	42.06-42.12	0.70	2.6	331
Robs 8	10154-02-08	43.06-43.09	0.81	2.4	333
Robs 9	10154-02-09	44.05-44.09	0.93	3.3	216

TABLE 4
RXTE SPECTRAL FITS FROM DEC. 1996 OBSERVATIONS

Observation	Phase	n_H $\times 10^{22} \text{cm}^{-2}$	Γ	Cutoff Energy keV	$F_{2-10\text{keV}}$ $\times 10^{-10} \text{ergs cm}^{-2} \text{s}^{-1}$	χ^2_ν
Robs1	0.995	$6.31^{+0.43}_{-0.43}$	$1.251^{+0.029}_{-0.029}$	$13.52^{+0.25}_{-0.25}$	2.92	0.63
Robs2	0.114	$2.38^{+0.49}_{-0.49}$	$1.255^{+0.038}_{-0.039}$	$14.00^{+0.41}_{-0.40}$	1.63	0.84
Robs3	0.233	$2.08^{+0.86}_{-0.89}$	$1.259^{+0.067}_{-0.070}$	$13.92^{+1.22}_{-0.87}$	0.89	0.92
Robs6	0.550	$2.68^{+0.28}_{-0.28}$	$1.184^{+0.022}_{-0.023}$	$13.47^{+0.21}_{-0.22}$	3.30	1.00
Robs7	0.671	$3.28^{+0.36}_{-0.35}$	$1.369^{+0.028}_{-0.029}$	$13.52^{+0.28}_{-0.29}$	4.41	1.50
Robs8	0.790	$7.89^{+0.29}_{-0.29}$	$1.415^{+0.020}_{-0.019}$	$13.50^{+0.16}_{-0.17}$	4.29	0.88
Robs9	0.909	$7.91^{+0.81}_{-0.77}$	$1.362^{+0.049}_{-0.048}$	$13.62^{+0.55}_{-0.49}$	1.21	0.72